Wang *et al. Microstructures* 2022;2:2022016
DOI: 10.20517/microstructures.2022.11

Microstructures

Research Article

Open Access

Check for updates

Ultrasonication-assisted fabrication of porous ZnO@C nanoplates for lithium-ion batteries

Xueting Wang[1], Yunchuang Wang[2], Meichao Wu[2], Ruopian Fang[1], Xi Yang[3], Da-Wei Wang[1]

[1]School of Chemical Engineering, The University of New South Wales, Sydney 2052, Australia.
[2]Key Laboratory of Functional Polymer Materials, College of Chemistry, Nankai University, Tianjin 300071, China.
[3]Institute of Chemical Materials, China Academy of Engineering Physics, Mianyang 621900, Sichuan, China.

Correspondence to: Prof. Da-Wei Wang, School of Chemical Engineering, The University of New South Wales, Sydney 2052, Australia. E-mail: da-wei.wang@unsw.edu.au

How to cite this article: Wang X, Wang Y, Wu M, Fang R, Yang X, Wang DW. Ultrasonication-assisted fabrication of porous ZnO@C nanoplates for lithium-ion batteries. *Microstructures* 2022;2:2022016. https://dx.doi.org/10.20517/microstructures.2022.11

Received: 19 May 2022 **First Decision:** 23 Jun 2022 **Revised:** 3 Jul 2022 **Accepted:** 18 Jul 2022 **Published:** 26 Jul 2022

Academic Editors: Jun Chen, Shiqing Deng **Copy Editor:** Fangling Lan **Production Editor:** Fangling Lan

Abstract

Lithium-ion batteries have made significant commercial and academic progress in recent decades. Zinc oxide (ZnO) has been widely studied as a lithium-ion battery anode due to its high theoretical capacity of 987 mAh g^{-1}, natural abundance, low cost, and environmental friendliness. However, ZnO suffers from poor electronic conductivity and large volume variation during the battery discharge/charge process, leading to capacity deterioration during long-term cycling. Herein, porous ZnO@C nanoplates are developed to offer short ion diffusion pathways and good conduction networks for both Li ions and electrons. The porous nanoplates provide abundant active sites for electrochemical reactions with minimized charge transfer impedance. As a result, the porous ZnO@C nanoplates deliver higher performance for lithium-ion storage compared with a bare ZnO anode. Furthermore, with the introduction of reduced graphene oxide (rGO), the ZnO@C@rGO composite anode achieves a capacity of 229.3 mAh g^{-1} at a high current density of 2 A g^{-1}.

Keywords: Zinc oxide, porous materials, lithium-ion batteries, anodes

INTRODUCTION

Lithium-ion batteries (LIBs), as mainstream energy storage technologies, have been widely used in electronic vehicles, portable devices, and energy storage power stations[1-3]. Traditional graphite anodes with

a low theoretical capacity of 372 mAh g^{-1} can barely satisfy the ever-increasing requirements for high-output LIBs[4]. Therefore, intensive efforts have been devoted to exploring high-capacity anode alternatives for high-energy-density LIBs. Zinc oxide (ZnO), with a high theoretical capacity of 987 mAh g^{-1} can be a potential anode material for next-generation LIBs, where it undergoes a reversible conversion reaction and an alloying-dealloying reaction during the electrochemical cycling process[5]. Despite its high potential capacity, ZnO anodes often suffer from poor electric conductivity, low chemical reaction kinetics, and an undesirable volume change (228%) during lithiation/delithiation, resulting in poor rate performance, electrode pulverization and rapid capacity fading during cycling[6,7]. To address these issues and enhance the electrochemical performance of ZnO-based anodes, strategies, including constructing nanoarchitectures, hybridizing ZnO with conductive materials, and combining two or more metal oxides with ZnO to prepare heterostructures, have been developed[8,9]. The construction of nanostructured ZnO materials has been studied intensively, owing to its effectiveness in boosting the electrochemical performance of ZnO anodes via the reduction of ion diffusion paths and the volume change accommodation during cycling. However, the methods of synthesizing ZnO nanostructures, such as hydro(solvo) thermal reactions and sol-gel and chemical vapor deposition, can be time-consuming and complex[10]. Furthermore, reduced graphene oxide (rGO), as a popular conductive matrix, has been proven to be efficient in facilitating electron transport, buffering volume expansion, and preventing the aggregation of metal oxide electrode materials during electrochemical cycling[11-13].

Herein, we report a facile strategy to fabricate ZnO@C nanoplates by a simple sonication reaction in a water-ethanol mixture avoiding the use of hazardous solvents, followed by calcination. The sonication process based on the mechanical, thermal, and chemical effects of acoustic cavitations has proven to be simple, time-saving, and efficient[14,15]. The porous ZnO@C composite offers a high surface area, which facilitates electrolyte penetration and accommodates the volume variation. Furthermore, the in-situ formed carbon coating on ZnO not only enhances the electronic conductivity but also prevents the active species from pulverization. As a result, the prepared ZnO@C composite delivers enhanced cycle and rate performance when applied as a lithium-ion battery anode compared with a bare ZnO electrode. After 100 cycles at 0.5 C (1 C = 1000 mA g^{-1}), the ZnO@C anode has a specific capacity of 207 mAh g^{-1}, while pristine ZnO only delivers a capacity of 56 mAh g^{-1}. At a high rate of 2 C, the ZnO@C composite can achieve a capacity of 77.6 mAh g^{-1}, whereas a 9.7 mAh g^{-1} capacity is obtained for the commercial ZnO material. In addition, ZnO@C@rGO composites are fabricated and a reversible capacity of 354 mAh g^{-1} is obtained after 100 cycles at 0.5 C. A good rate performance is also achieved with a capacity of 229.3 mAh g^{-1} at a high rate of 2 C.

MATERIALS AND METHODS

Materials

All the chemicals were used as received without further purification, including ZnO nanopowder (ZnO, Sigma-Aldrich, < 100 nm, 15-20 m^2 g^{-1}), trimesic acid (H_3BTC, Aladdin, 98%), ethanol absolute (EtOH > 95%) and distilled water.

Sample preparation and characterization

Synthesis of ZnO@C nanoplates

The preparation process of the ZnO@C nanoplates is illustrated in Figure 1. Firstly, ZnO-H_3BTC nanoplate intermediates were prepared by a simple ultrasonication method at room temperature. In a typical process, 162 mg of ZnO nanoparticles and 84 mg of H_3BTC were dispersed in a mixture of H_2O and EtOH (60 mL, v/v = 1/1) by ultrasonication for 4 h. The obtained white product was washed with water and EtOH three times by centrifugation. The ZnO-H_3BTC intermediates were obtained after drying at 80 °C for 6 h. The ZnO@C composites were prepared by annealing the ZnO-H_3BTC intermediates at 500 °C for 4 h with a

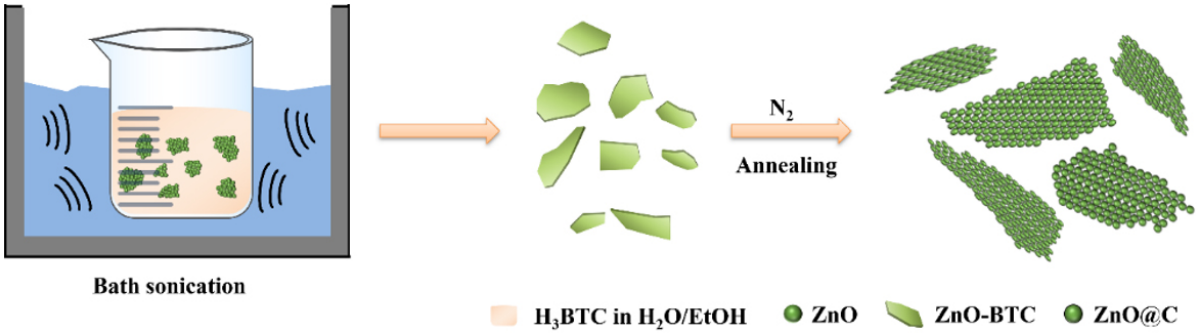

Figure 1. Illustration of fabrication of plate-like porous ZnO@C composites.

heating rate of 2 °C per minute under a N_2 atmosphere in a tube furnace.

Structural and morphological characterization

The phases of the materials were identified by powder X-ray diffraction (XRD) via an Ultima IV X-ray diffractometer (Rigaku) with Cu Kα radiation. The data were collected from powder samples at a scanning rate of 10° per min for 2θ in the range of 3°-80°. Raman spectra were obtained on a WITec alpha300 confocal Raman microscope. Scanning electron microscopy (SEM) and energy-dispersive X-ray spectroscopy were conducted on a TESCAN MIRA LMS. Transmission electron microscopy (TEM), high-resolution TEM (HRTEM), and selected area electron diffraction (SAED) were conducted on a FEI Tecnai F30 microscope. The Brunauer-Emmett-Teller (BET) surface area was measured on a Micromeritics ASAP 2020 surface area and porosity analyzer. Fourier transform infrared (FT-IR) spectra were collected using a BRUKER Tensor 27 on a KBr pellet in the wavenumber range of 500-4000 cm^{-1}. Thermogravimetric analysis (TGA) was recorded on a TG50 analyzer (Mettler Toledo).

Electrochemical characterization

To measure the electrochemical performance of the obtained composites, CR2025 coin cells were assembled. Typically, the active materials, polyvinylidene fluoride, and Super P were mixed in an agate mortar with a weight ratio of 8:1:1 by grinding them together with N-methyl pyrrolidone. Afterwards, the obtained smooth slurry was coated on a Cu foil (10 μm thick) current collector using a doctor blade. After drying at 80 °C under a vacuum for 12 h, the electrode sheets were pressed and punched into 10 mm-diameter circular working electrodes with a mass loading of 1-2 mg cm^{-2}. The CR2025 coin cells were assembled in a glove box (oxygen < 0.01 ppm and H_2O < 0.01 ppm) with a Li disk (14 × 0.4 mm) as the reference and counter electrode. A Celgard 2325 membrane was applied as the separator and 1 M $LiPF_6$ in 1:1:1 (v/v/v) ethylene carbonate/dimethyl carbonate/ethyl methyl carbonate (EC/DMC/EMC) was used as the electrolyte. The assembled coin cells were rested for 12 h before the subsequent electrochemical testing. A LAND CT2001A battery test system was used to record the galvanostatic charge-discharge curves, rate performance, and cycling stability of the cells. Cyclic voltammetry (CV) and electrochemical impedance spectroscopy (EIS) were carried out using a Metronhm Autolab Nova 2.0.1 electrochemical workstation. The impedance spectra were recorded in the frequency range of 1 MHz to 0.01 Hz with an AC voltage of 5 mV. The CV measurements were conducted at various scan rates in potential ranges of 0.01-3.0 V.

RESULTS AND DISCUSSION

The obtained ZnO@C composites and ZnO-H_3BTC intermediates were characterized by XRD, as shown in Figure 2A. The ZnO-H_3BTC intermediates prepared by the reaction between ZnO and H_3BTC under ultrasonication displayed new peaks besides the residual ZnO peaks, as labeled by the blue clubs at 7.2°, 9.0°,

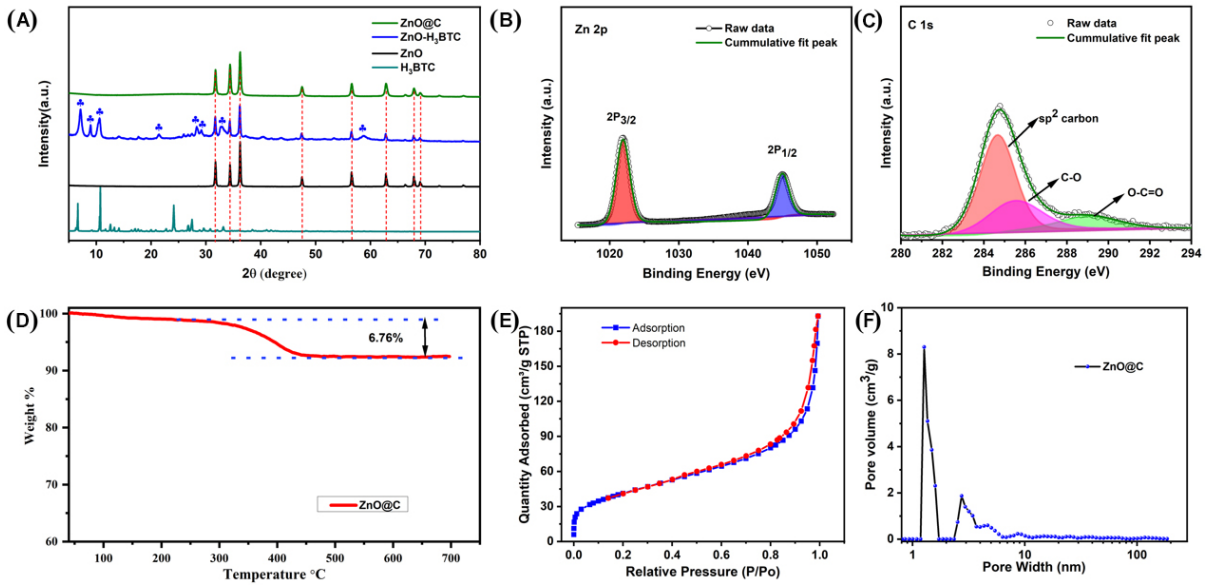

Figure 2. Structural characterization of prepared ZnO@C materials. (A) XRD patterns of commercial ZnO and H_3BTC, ZnO-H_3BTC intermediates and ZnO@C products. (B) Zn 2p and (C) C 1s spectra of ZnO@C composites. (D) TGA curve of ZnO@C under air atmosphere with a heating rate of 10 °C min^{-1} from 40 to 700 °C. (E) Nitrogen adsorption-desorption isotherms and (F) corresponding pore-size distribution of ZnO@C composites. XRD: X-ray diffraction.

10.6°, 21.5°, 28.3°, 29.2°, 31.7°, and 58.7°. This suggests the partial etching of ZnO under the sonication at room temperature. TGA [Supplementary Figure 1], FT-IR spectroscopy [Supplementary Figure 2], and XPS [Supplementary Figure 3] also confirmed the successful etching reaction of the ZnO-H_3BTC material. After calcination, the intermediates turned into ZnO@C with peaks of only ZnO at 31.8°, 34.4°, 36.2°, 47.6°, 56.6°,62.9°, 66.4°, 67.9° and 69.1°, corresponding to the (100), (002), (101), (102), (110), (103), (200), (112) and (201) planes of zincite (PDF #36-1451), respectively. The absence of carbon peaks in the ZnO@C products may result from the amorphous nature of carbon derived from the intermediates and/or the low content of carbon in the ZnO@C composites.

XPS was conducted to detect the surface chemistry of the ZnO@C composites. The survey spectra displayed in Supplementary Figure 4A confirmed that ZnO@C was composed of Zn, O, and C. Figure 2B shows the high-resolution Zn 2p spectrum with two obvious peaks at 1022 and 1045 eV, corresponding to the $2p_{3/2}$ and $2p_{1/2}$ of Zn, respectively[16]. The C 1s spectrum is shown in Figure 2C, where the peak at 284.5 eV was associated with sp^2 carbon. The peaks at 285.0 and 289.2 eV can be assigned to the C-O and O-C=O bonds, respectively[17]. Supplementary Figure 4B shows the deconvoluted O 1s spectrum. Three peaks at 531.2, 532.6, and 533.7 eV are observed, corresponding to the Zn-O, C-O, and O-C=O bonds, respectively[18].

TGA was carried out to determine the carbon content in the as-prepared ZnO@C. The main weight loss at ~200 to 450 °C is related to carbon combustion in air, which was calculated to be 6.76 wt.%, as shown in Figure 2D. The BET surface area of the ZnO-H_3BTC-derived ZnO@C composites was determined by nitrogen adsorption-desorption isotherms. Figure 2E and F display the isotherm curves, as well as the corresponding pore size distribution calculated by the Barrett-Joyner-Halenda method. The BET specific surface area of the ZnO@C nanosheets was 150.65 $m^2 g^{-1}$, which was much higher than the ZnO-BTC (30.55 $m^2 g^{-1}$, Supplementary Figure 5) and commercial ZnO (15-20 $m^2 g^{-1}$). Furthermore, the pore size distributions of the ZnO@C suggested that the pores were mainly micropores and mesopores. The abundant surface area and porous structures of ZnO@C composites are conducive to the accommodation of

volume variations and the exposure of electrochemical reaction sites for lithium-ion transfer during battery cycling[19,20].

The morphological features of the as-prepared ZnO@C were firstly characterized via SEM. As shown in Figure 3A, the ZnO@C inherited the plate-like morphology of the ZnO-BTC intermediates [Supplementary Figure 6], suggesting that the plate morphology can be well preserved during the thermal decomposition. The nanoplates were formed by densely packed nanoparticles [Figure 3B]. Figure 3C displays the elemental mapping images of the ZnO@C composites, indicating the uniform distribution of Zn, O, and C elements in the composites. The TEM image in Figure 3D illustrates that the nanoparticles had a particle size of several nanometers. This unique porous and hierarchical structure can facilitate electrolyte infiltration and Li^+ transport and accommodate the volume change during the repeated charge/discharge process. The HRTEM image [Figure 3E] shows a clear lattice fringe with a crystalline interplanar spacing value (d) of 0.191 nm, corresponding to the (102) crystal face of ZnO. Furthermore, an amorphous carbon layer was observed on the ZnO nanoparticles resulting from the thermal annealing-induced in-situ carbon coating. The well-attached carbon coating on ZnO not only increases the electron conductivity but also buffers the volume change during the charge/discharge process of the ZnO anode[21]. The SAED image, as depicted in Figure 3F, indicates the polycrystalline nature of the ZnO@C composites. The well-defined diffraction rings correspond to the (210), (103), (110), (102), (002), and (100) planes, in agreement with the XRD.

The discharge-charge curves and corresponding differential capacity *vs.* voltage plots of the ZnO@C composites recorded at a current density of 0.1 C for the initial five cycles are displayed in Figure 4. The rate performance of the ZnO@C composites obtained by annealing ZnO-BTC at 500 °C for different times of 2, 4, and 6 h is displayed in Supplementary Figure 7. The 4 h annealing time resulted in the ZnO@C composite demonstrating the highest capacity at all current densities; thus, this composite was used for the subsequent studies. In the first discharge process, the reduction peak starting from ~0.95 V was assigned to the reduction of ZnO by Li to metallic Zn, accompanied by the generation of Li_2O [Eq. (1)][5]. The reduction peak located at ~0.6 V was the electrolyte decomposition and SEI formation, which was irreversible and did not appear in the subsequent cycles[22]. The alloy reaction between lithium and zinc occurred in a multi-step manner. The formation of Li_xZn ($0 < x < 1$) and LiZn occurred at 0.45 and 0.07 V, respectively [Eq. (2)][23]. In the charge process, the four oxidation peaks located at 0.28, 0.36, 0.54, and 0.69 V correspond to the multi-step dealloying process of LiZn (LiZn, Li_2Zn_3, $LiZn_2$ and Li_2Zn_5)[24,25]. The broad anodic peak at 1.30 V can be assigned to the decomposition of Li_2O and the reformation of ZnO[26]. In the second lithiation process, the ZnO reduction started at a higher potential of 1.2 V, which may be due to the electrode activation after the first cycle. This peak shifted 0.09 V from 0.84 to 0.75 V from the 2nd to 5th cycle with an intensity decrease, suggesting an overpotential increase and capacity decay of the composite electrode during repeat cycling. On the other side, there existed a considerable ZnO reduction voltage shift of 0.165 V from 0.920 to 0.755 V in the lithiation process from the 2nd to 5th cycle, with a more dramatic intensity drop for the commercial ZnO electrode [Supplementary Figure 8], suggesting its faster overpotential accumulation and severer electrode polarization.

$$ZnO + 2Li^+ + 2e^- \rightarrow Zn + Li_2O \quad (1)$$

$$Zn + Li^+ + e^- \rightarrow LiZn \quad (2)$$

The electrochemical performance of the ZnO@C composites and bare ZnO as lithium-ion battery anodes was evaluated.

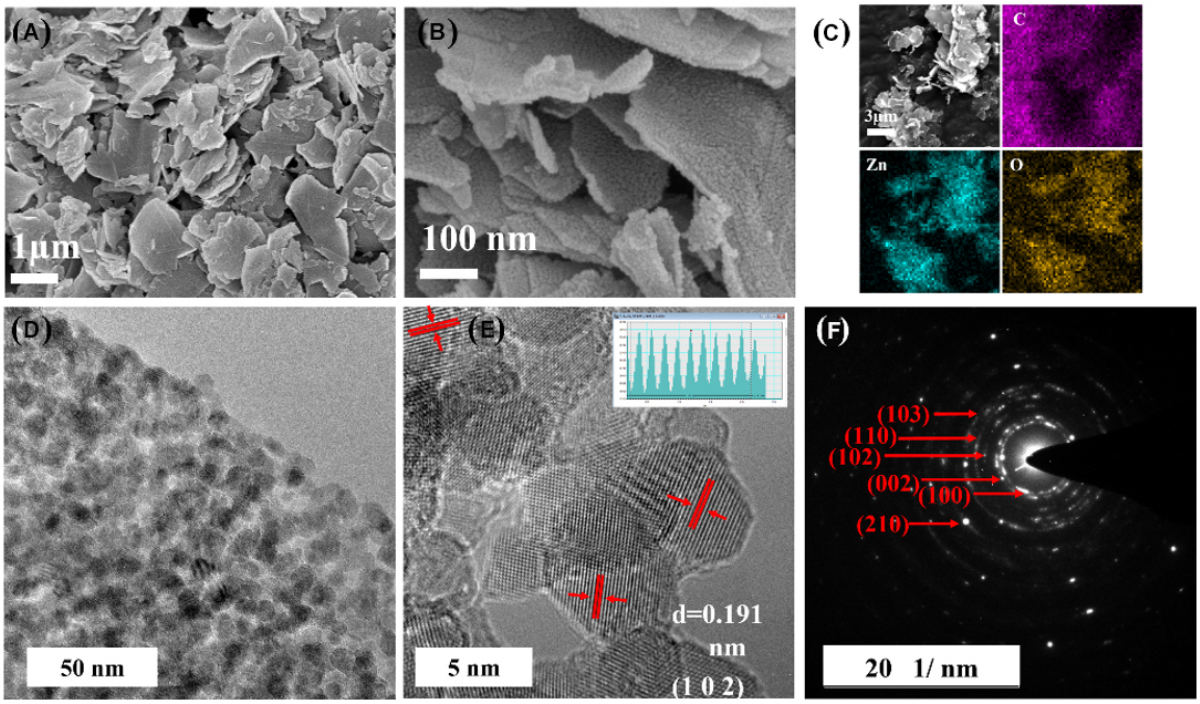

Figure 3. Morphological characterization of ZnO@C materials. (A and B) SEM images, (C) elemental mapping images, (D) TEM image, (E) HRTEM image, and (F) SAED analysis of ZnO@C composites.

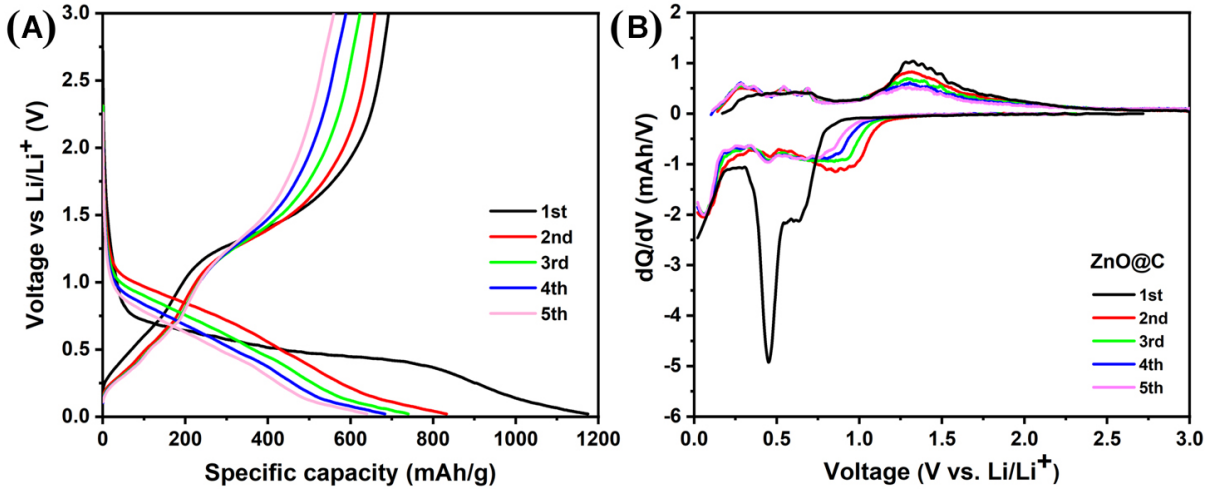

Figure 4. (A) Discharge-charge curves and (B) differential capacity vs. voltage (dQ/dV) plots of ZnO@C composites for the initial five cycles at a current density of 0.1 C.

Figure 5A displays the rate performance of the electrodes based on ZnO@C composites and commercial ZnO nanoparticles at various current densities. Clearly, the ZnO@C composite-based electrode delivered much higher specific capacities than the pristine ZnO electrode at all current densities, suggesting the better rate capability of the composite electrode. At 0.1 C, pristine ZnO showed initial capacities of 863/461 mAh g^{-1} with an initial Coulombic efficiency (CE) of 53% [Figure 5B]. In contrast, the ZnO@C composites delivered initial discharge/charge capacities of 1175/700 mAh g^{-1} with a CE of 60% [Figure 5C]. Both electrodes showed low CEs in the initial cycles, but their CEs increased to ~96% after five cycles and

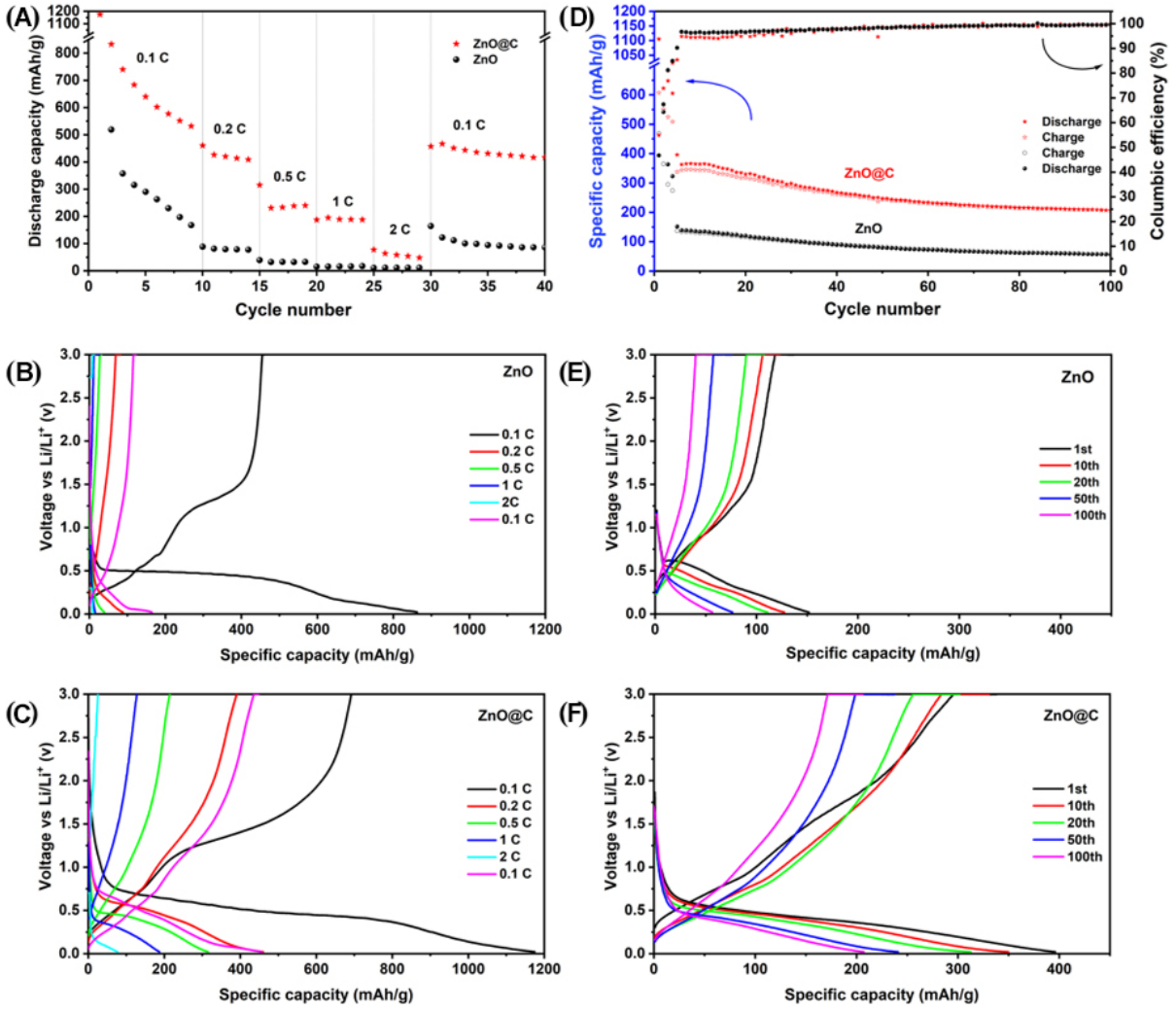

Figure 5. Electrochemical performance comparison of commercial ZnO and prepared ZnO@C materials. (A) Rate capability and (B and C) corresponding discharge-charge curves. (D) Cycle performance and (E and F) corresponding discharge-charge curves.

then increased to over 99% in successive cycles. The low initial CEs can be ascribed to the formation of an immense SEI, as well as possible crystal coarsening[27,28]. For the ZnO@C anode, its high specific surface area inevitably induces a large adsorption surface and thus enormous electrolyte decomposition accompanying the SEIs[29]. The discharge capacities of the ZnO@C composite at 0.2 C, 0.5 C, 1 C, and 2 C were 460.3, 315.4, 187.3, and 77.6 mAh g^{-1}, respectively. In contrast, the ZnO electrodes exhibited inferior performance and delivered lower specific capacities of only 110.4, 54.4, 14.9, and 9.7 mAh g^{-1}, respectively. When the current density was recovered to 0.1 C, the reversible capacity of the ZnO@C composite increased to 450 mAh g^{-1}, while ZnO had a capacity of only 122 mAh g^{-1}. The improved capacity of the ZnO@C nanosheets compared with pristine ZnO can mainly be ascribed to the following aspects: (1) ZnO@C has a higher specific surface area (150 m^2 g^{-1}) than pristine ZnO (15-20 m^2g^{-1}), which can provide more electrochemical active sites[30,31]; (2) The porous structure of ZnO@C is also beneficial for ion transport and the conductive carbon coating ensures efficient electrical contact through the electrode. These features are beneficial for the improved kinetics of electrochemical reactions, which thus contribute to improved active material utilization[8,31,32].

Figure 5D shows a cycling performance comparison between the ZnO@C and pristine ZnO materials investigated at a current density of 0.5 C after five pre-activation cycles at 0.1 C. Figure 5E and F show the corresponding charge-discharge curves of the two materials. The ZnO@C composites exhibited a high discharge capacity of 396 mAh g^{-1}, with a capacity of 207.2 mAh g^{-1} achieved after 100 cycles. However, for the commercial ZnO nanoparticles, the discharge capacities were only 151.7 and 56.4 mAh g^{-1} before and after 100 cycles, respectively. In addition, the voltage gaps between the charge and discharge curves of ZnO@C were much smaller than that of the ZnO anode materials, as shown in Supplementary Figure 9, indicating the lower transport resistance and smaller polarization of the ZnO@C electrodes[33]. The electrochemical enhancement of the ZnO@C composites can be ascribed to the carbon coating, smaller particle size and the improved specific area of the composite material compared with bare ZnO, as discussed above. To further understand the storage mechanism of the ZnO@C anode, CV was conducted under different scan rates from 0.2 to 2.0 mV/s, as shown in Supplementary Figure 10A. The lithium storage mechanism could be divided into diffusion-controlled behavior and capacitive storage, which could be estimated according to:

$$i = a\nu^{b} \quad (3)$$

$$\log(i) = b\log(\nu) + \log(a) \quad (4)$$

Generally, when b is close to 0.5, the process is diffusion controlled. In contrast, when b approaches unity, the process is capacitance controlled[34-36].

Supplementary Figure 10B shows the relationship between log (i) and log (ν) and the b values corresponding to peaks 1 and 2 were 0.61 and 0.86, respectively. This result suggests that the lithium storage behavior of ZnO@C was controlled by a synergic effect of diffusion and a capacitive process. The capacitive process contribution for the ZnO@C anode was calculated according to:

$$i(\nu) = k_1\nu + k_2\nu^{1/2} \quad (5)$$

where $k_1\nu$ accounts for the current contributed from the capacitive process and $k_2\nu^{1/2}$ corresponds to the current coming from the diffusion process[37-39].

The capacitive contribution was determined to be 76.3% at a scan rate of 0.8 mV/s [Supplementary Figure 10C]. Supplementary Figure 10D shows that the percentage of capacitance contribution grew with the increasing scan rate. Specifically, the capacitive contributions were 61.6%, 71.8%, 78.2% and 83.6% at scan rates of 0.2, 0.5, 1 and 2 mV/s, respectively. Therefore, the capacitive process played a vital role in the total capacity of the ZnO@C anode.

The inferior rate and cycle performance of ZnO could be related to its larger particle size, poor electronic conductivity and the drastic volume change during the electrochemical charge/discharge process. ZnO@C nanoplates derived from ZnO-BTC nanoplates that served as a sacrificial template and precursor possessed a high surface area that was conducive to the exposure of active sites for the electrochemical reaction. The carbon coating ensured good electronic conductivity, sufficient lithium-ion permeability, and electrochemical stability. Furthermore, the structure of metal oxide embedded in porous carbon matrices was able to facilitate the transportation of electrons and ions, as well as relieve the stress induced during cycling[40-42].

EIS was employed to study the charge transfer behavior and interfacial properties of the electrodes. EIS tests were carried out in the fresh state and after 100 cycles at 0.5 C for both electrodes. As shown in Figure 6A, the Nyquist plots were all composed of two partly overlapped semicircles and a sloping line. The semicircle located in the high-frequency region was related to surface film impedance and the second one that appeared at the middle frequency corresponded to the charge transfer resistance. In the low-frequency region, there existed a slopping line known as the Warburg impedance region, which referred to the lithium-ion diffusion in the bulk electrode[43]. The EIS data were fitted with the equivalent circuit in Supplementary Figure 11 and the fitting results were plotted in Figure 6B. R_s, the ohmic resistance, was related to the intrinsic resistance composed of the resistance of the electrode material, the ionic resistance of the electrolyte, and the contact resistance between the electrode and current collector[44]. R_1 and CPE_1 were assigned to the resistance of the SEI layer and the corresponding constant phase angle element. R_2 and CPE_2 represent the charge transference resistance and corresponding constant phase angle element and Z_w was the Warburg impedance[45]. For the ZnO anode, after 100 cycles, the R_s, R_1, and R_2 values all increased to some extent [Figure 6B], especially R_1, which may be attributed to constant SEI reformation and accumulation during long-term cycling. In contrast, for the ZnO@C electrode, the R_s and R_2 decreased after the electrochemical charge/discharge process, which may result from the better electrolyte wettability of the electrode and/or activation of the electrode along with electrochemical cycling. The increase of R_1 for the ZnO@C electrodes after cycling was negligible. Furthermore, after 100 cycles, the ZnO@C composite electrode possessed a much lower interfacial resistance (4.64 Ω) than that of ZnO (44.6 Ω), and an obviously smaller charge transfer resistance of 48.54 Ω for ZnO@C and 216.3 Ω for ZnO, indicating that the ZnO@C composite-based electrode exhibited faster charge transfer[46]. EIS spectra were also applied to compare the lithium diffusion coefficient of two materials with the details described in the supporting information [Supplementary Figure 12]. The higher lithium-ion diffusion coefficient of the ZnO@C electrodes allowed fast lithium diffusion and thus good rate performance. These EIS results were consistent with the cycle and rate performance discussed above.

Despite the improvement, the electrochemical performance of the ZnO@C composite electrode was not satisfactory, which may be due to the low carbon content of only above 6%. rGO has been demonstrated to be effective in improving the electrochemical performance of metal oxide anodes, resulting from its electronic conductivity along with the ability to accommodate the drastic volume change of the electrode materials[47,48]. Therefore, rGO was introduced to further boost the electrode performance and the detailed preparation and characterization of ZnO@C@rGO were described in the supporting information [Supplementary Figures 13 and 14]. The rate capabilities and cycle performance of the as-prepared ZnO@C@rGO-based electrodes were evaluated, as depicted in Figure 7. As expected, ZnO@C@rGO delivered enhanced electrochemical performance due to the improved conductivity and volume change mitigation ability. To be specific, the ZnO@C@rGO composites electrode was able to deliver a high specific capacity of 414.7 mAh g^{-1} after 50 cycles at 0.5 C, corresponding to a capacity retention of 80%, much higher than that of the ZnO@C electrode (241 mAh g^{-1}, retention of 60.8%). Even after 100 cycles, a reversible capacity of 354 mAh g^{-1} was obtained by ZnO@C@rGO electrodes. In addition, a smaller voltage gap between charge-discharge curves can be observed in the corresponding charge-discharge curves [Figure 7B] of ZnO@C@rGO compared with those of ZnO@C electrodes both before and after 100 cycles, implying much decreased polarization resulted from the introduction of rGO. The rate capability of the ZnO@C@rGO composites was measured at the same condition as the ZnO@C electrodes, as depicted in Figure 7C and D. After 10 cycles at 0.1 C, a reversible capacity of 640.4 mA g^{-1} was obtained for the ZnO@C@rGO composites. It delivered specific capacities of 573.1, 473.3, 344, and 229.3 mAh g^{-1} at 0.2 C, 0.5 C, 1 C, and 2 C, respectively. Moreover, when the current density is converted back to 0.1 C, the specific capacity of ZnO@C@rGO can recover to 608.3 mAh g^{-1}. The superior electrochemical performance of ZnO@C@rGO can be attributed to the introduction of rGO and the good distribution of ZnO@C on the

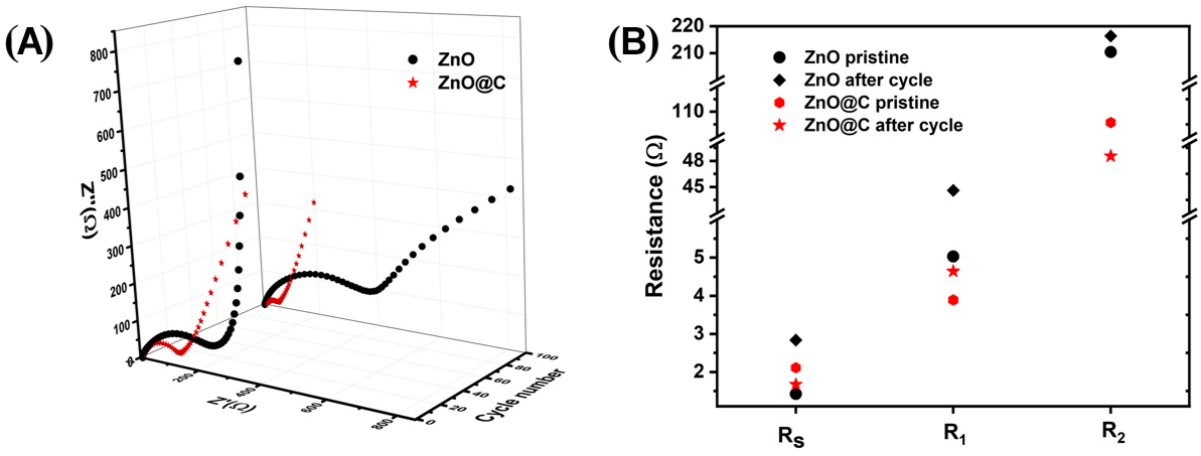

Figure 6. (A) EIS curves of ZnO and ZnO@C anodes before and after 100 cycles at 0.5 C in the frequency range of 1 MHz to 0.01 Hz. (B) Resistance values of electric elements simulated from EIS spectra.

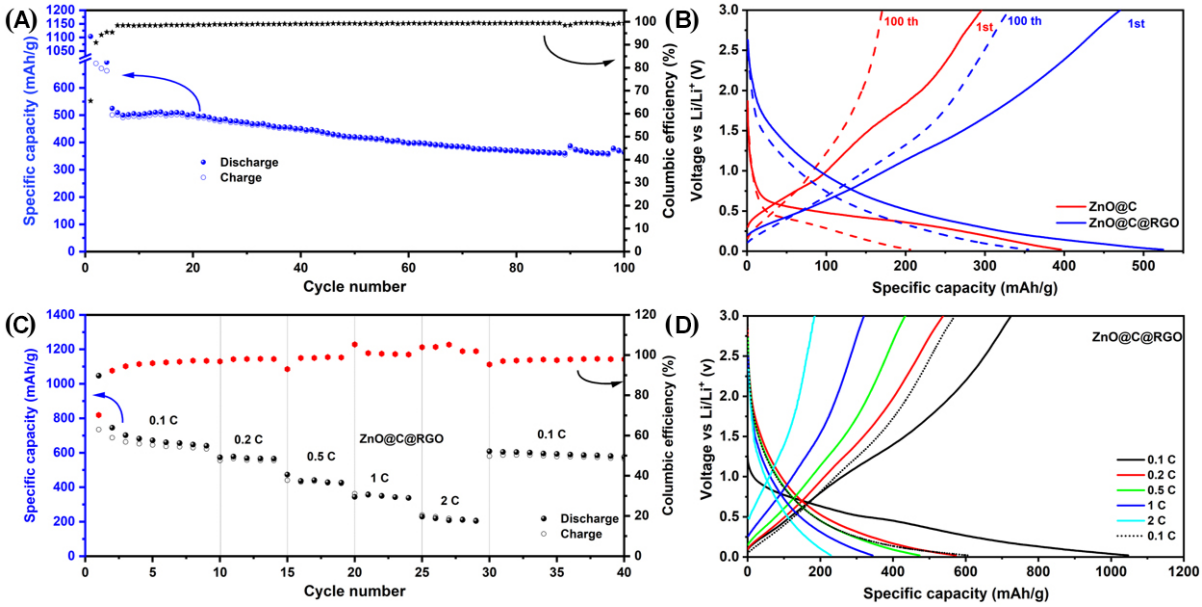

Figure 7. Electrochemical performance of ZnO@C@rGO. (A) Cycle performance at 0.5 C and (B) corresponding charge-discharge curves. (C) Rate capability and (D) corresponding charge-discharge curves of ZnO@C@rGO electrodes.

wrinkled graphene sheets.

CONCLUSIONS

In summary, porous nanoplates assembled by ZnO@C nanoparticles were developed via a facile sonication reaction and applied as lithium-ion battery anode materials. By ultrasonication of ZnO and trimesic acid in a mixed solvent of water and ethanol, ZnO-BTC intermediates were obtained. The plate morphology was successfully inherited by its derivative ZnO@C composites, synthesized by simply thermal annealing under an inert atmosphere. This ZnO-BTC derived ZnO@C composite electrode delivered an improved electrochemical performance compared with bare ZnO when applied as anode materials for LIBs. Firstly, the abundant surface area of the composite with a 2D morphology was beneficial for the exposure of active

electrochemical sites and facilitating the ion and electron transport during charge/discharge. Secondly, the in-situ formed carbon coating during pyrolysis can greatly improve the electronic conductivity and release the stress caused by the volume change of the ZnO electrode. To further enhance the electrochemical performance of the ZnO@C anode, rGO was introduced and a capacity of 229.3 mAh g^{-1} was achieved for the ZnO@C@rGO-based electrode at a high current density of 2 A g^{-1}. This context presented a facile and efficient method to prepare carbon coated metal oxide as lithium-ion battery anode material with 2D morphology, and this strategy could be possibly extended to fabricate other electrode materials for energy storage.

DECLARATIONS

Authors' contributions

Performed materials synthesis, electrochemical experiments, data collection and analysis, manuscript drafting: Wang X
Contributed to the conception and design of the materials: Wang Y, Yang X
Helped with material preparation and characterization: Wu M
Contributed to manuscript revision and mechanism explanation: Fang R
Supervised the overall project: Wang DW
All authors have given approval to the final version of the manuscript.

Availability of data and materials

Data can be deposited into data repositories or published as supplementary information in the journal.

Financial support and sponsorship

This work was financially supported by the Australian Research Council Discovery Project (DP190101008); Future Fellowship (FT190100058); DECRA (DE210101157) and Stipend Scholarship from China Scholarship Council.

Conflicts of interest

All authors declared that there are no conflicts of interest.

Ethical approval and consent to participate

Not applicable.

Consent for publication

Not applicable.

REFERENCES

1. Hayner CM, Zhao X, Kung HH. Materials for rechargeable lithium-ion batteries. *Annu Rev Chem Biomol Eng* 2012;3:445-71. DOI PubMed
2. Wu F, Maier J, Yu Y. Guidelines and trends for next-generation rechargeable lithium and lithium-ion batteries. *Chem Soc Rev* 2020;49:1569-614. DOI PubMed
3. Qian S, Xing C, Zheng M, et al. $CuCl_2$-modified lithium metal anode via dynamic protection mechanisms for dendrite-free long-life charging/discharge processes. *Adv Energy Mater* 2022;12:2103480. DOI
4. Zhang J, Tan T, Zhao Y, Liu N. Preparation of ZnO nanorods/graphene composite anodes for high-performance lithium-ion batteries. *Nanomaterials* 2018;8:966. DOI PubMed PMC
5. Kreissl JJA, Petit J, Oppermann R, et al. Electrochemical lithiation/delithiation of Zno in 3D-structured electrodes: elucidating the mechanism and the solid electrolyte interphase formation. *ACS Appl Mater Interfaces* 2021;13:35625-38. DOI PubMed

6. Lai W, Li X, Li B, et al. MOF-derived ZnO/ZnFe2O4@RGO nanocomposites with high lithium storage performance. *J Solid State Electrochem* 2021;25:1175-81. DOI
7. Thauer E, Zakharova GS, Andreikov EI, et al. Novel synthesis and electrochemical investigations of ZnO/C composites for lithium-ion batteries. *J Mater Sci* 2021;56:13227-42. DOI
8. Bui VKH, Pham TN, Hur J, Lee YC. Review of ZnO binary and ternary composite anodes for lithium-ion batteries. *Nanomaterials (Basel)* 2021;11:2001. DOI PubMed PMC
9. Köse H, Dombaycıoğlu Ş, Aydın AO. Graphene-based architectures of tin and zinc oxide nanocomposites for free-standing binder-free Li-ion anodes. *Int J Energy Res* 2018;42:4710-8. DOI
10. Wang L, Zhang G, Liu Q, Duan H. Recent progress in Zn-based anodes for advanced lithium ion batteries. *Mater Chem Front* 2018;2:1414-35. DOI
11. Wang K, Ye W, Yin W, Chai W, Rui Y, Tang B. Several carbon-coated Ga_2O_3 anodes: efficient coating of reduced graphene oxide enhanced the electrochemical performance of lithium ion batteries. *Dalton Trans* 2021;50:3660-70. DOI PubMed
12. Zou Y, Guo Z, Ye L, et al. Co/La-Doped NiO hollow nanocubes wrapped with reduced graphene oxide for lithium storage. *ACS Appl Nano Mater* 2021;4:2910-20. DOI
13. Kim C, Kim JW, Kim H, et al. Graphene oxide assisted synthesis of self-assembled zinc oxide for lithium-ion battery anode. *Chem Mater* 2016;28:8498-503. DOI
14. Noman MT, Petru M, Amor N, Louda P. Thermophysiological comfort of zinc oxide nanoparticles coated woven fabrics. *Sci Rep* 2020;10:21080. DOI PubMed PMC
15. Vaitsis C, Sourkouni G, Argirusis C. Metal organic frameworks (MOFs) and ultrasound: a review. *Ultrason Sonochem* 2019;52:106-19. DOI PubMed
16. Zhao J, Zhou H, Jin M, Chen P, Chen S, Liu X. ZnO/TiO2/C nanofibers by electrospinning for high-performance lithium storage. *J Mater Sci* 2021;56:2497-505. DOI
17. Yan X, Xu S, Wang Q, Fan X. Activated carbon fibers "thickly overgrown" by ag nanohair through self-assembly and rapid thermal annealing. *Nanoscale Res Lett* 2017;12:590. DOI PubMed PMC
18. Guo C, Wang Q, He J, et al. Rational design of unique ZnO/ZnS@N-C heterostructures for high-performance lithium-ion batteries. *J Phys Chem Lett* 2020;11:905-12. DOI PubMed
19. Fu H, Liu Y, Chen L, et al. Designed formation of $NiCo_2O_4$ with different morphologies self-assembled from nanoparticles for asymmetric supercapacitors and electrocatalysts for oxygen evolution reaction. *Electrochimica Acta* 2019;296:719-29. DOI
20. Han Y, Qi P, Li S, et al. A novel anode material derived from organic-coated ZIF-8 nanocomposites with high performance in lithium ion batteries. *Chem Commun (Camb)* 2014;50:8057-60. DOI PubMed
21. Song Y, Chen Y, Wu J, et al. Hollow metal organic frameworks-derived porous ZnO/C nanocages as anode materials for lithium-ion batteries. *J Alloys Comp* 2017;694:1246-53. DOI
22. Mueller F, Geiger D, Kaiser U, Passerini S, Bresser D. Elucidating the impact of cobalt doping on the lithium storage mechanism in conversion/alloying-type zinc oxide anodes. *ChemElectroChem* 2016;3:1311-9. DOI
23. Xiao L, Mei D, Cao M, Qu D, Deng B. Effects of structural patterns and degree of crystallinity on the performance of nanostructured ZnO as anode material for lithium-ion batteries. *J Alloys Comp* 2015;627:455-62. DOI
24. Lu X, Xie A, Jiang C, et al. Synthesis of well-dispersed ZnO-Co-C composite hollow microspheres as advanced anode materials for lithium ion batteries. *RSC Adv* 2017;7:4269-77. DOI
25. Yu M, Wang A, Wang Y, Li C, Shi G. An alumina stabilized ZnO-graphene anode for lithium ion batteries via atomic layer deposition. *Nanoscale* 2014;6:11419-24. DOI PubMed
26. Zhou Z, Zhang K, Liu J, Peng H, Li G. Comparison study of electrochemical properties of porous zinc oxide/N-doped carbon and pristine zinc oxide polyhedrons. *J Power Sources* 2015;285:406-12. DOI
27. Guo R, Huang X, Wu J, Zhong W, Lin Y, Cao Y. ZnO/C nanocomposite microspheres with capsule structure for anode materials of lithium ion batteries. *Ceramics Int* 2020;46:19966-72. DOI
28. Ao L, Wu C, Xu Y, et al. A novel Sn particles coated composite of SnO/ZnO and N-doped carbon nanofibers as high-capacity and cycle-stable anode for lithium-ion batteries. *J Alloys Comp* 2020;819:153036. DOI
29. Song H, Su J, Wang C. In situ subangstrom-thick organic engineering enables mono-scale, ultrasmall Zno nanocrystals for a high initial coulombic efficiency, fully reversible conversion, and cycle-stable li-ion storage. *Adv Energy Mater* 2019;9:1900426. DOI
30. Ren P, Chen C, Yang X. Nanostrucutured MnO_2-TiN nanotube arrays for advanced supercapacitor electrode material. *Sci Rep* 2022;12:2088. DOI PubMed PMC
31. Theerthagiri J, Salla S, Senthil RA, et al. A review on ZnO nanostructured materials: energy, environmental and biological applications. *Nanotechnology* 2019;30:392001. DOI PubMed
32. Tao H, Zhou M, Wang K, Cheng S, Jiang K. Glycol derived carbon-TiO_2 as low cost and high performance anode material for sodium-ion batteries. *Sci Rep* 2017;7:43895. DOI PubMed PMC
33. Chen L, Jiang X, Wang N, Yue J, Qian Y, Yang J. Surface-amorphous and oxygen-deficient Li_3VO_4.. δ ;2:1500090. DOI PubMed PMC
34. Song Y, Cao Y, Wang J, et al. Bottom-up approach design, band structure, and lithium storage properties of atomically thin γ-FeOOH nanosheets. *ACS Appl Mater Interfaces* 2016;8:21334-42. DOI PubMed
35. Shi Y, Fu J, Hui K, et al. Promoting the electrochemical properties of yolk-shell-structured CeO_2 composites for lithium-ion batteries.

Microstructures 2021;1:2021005. DOI

36. Wu L, Liu YG, Zhao H, et al. MOF-derived long spindle-like carbon-coated ternary transition-metal-oxide composite for lithium storage. *ACS Omega* 2022;7:16837-46. DOI PubMed PMC
37. Liu J, Zhou Y, Xie Z, et al. Conjugated copper-catecholate framework electrodes for efficient energy storage. *Angew Chem Int Ed Engl* 2020;59:1081-6. DOI PubMed
38. Song Y, Chen Z, Li Y, et al. Pseudocapacitance-tuned high-rate and long-term cyclability of $NiCo_2S_4$ hexagonal nanosheets prepared by vapor transformation for lithium storage. *J Mater Chem A* 2017;5:9022-31. DOI
39. Yuan D, Adekoya D, Dou Y, et al. Cation-vacancy induced Li+ intercalation pseudocapacitance at atomically thin heterointerface for high capacity and high power lithium-ion batteries. *J Energy Chem* 2021;62:281-8. DOI
40. Li Y, Xu Y, Yang W, Shen W, Xue H, Pang H. MOF-Derived metal oxide composites for advanced electrochemical energy storage. *Small* 2018;14:e1704435. DOI PubMed
41. Xu G, Nie P, Dou H, Ding B, Li L, Zhang X. Exploring metal organic frameworks for energy storage in batteries and supercapacitors. *Mater Today* 2017;20:191-209. DOI
42. Muraliganth T, Vadivel Murugan A, Manthiram A. Facile synthesis of carbon-decorated single-crystalline Fe3O4 nanowires and their application as high performance anode in lithium ion batteries. *Chem Commun (Camb)* 2009:7360-2. DOI PubMed
43. Yang C, Qing Y, An K, et al. ZnO nanoparticles anchored on nitrogen and sulfur co-doped graphene sheets for lithium-ion batteries applications. *Ionics* 2018;24:3781-91. DOI
44. Li D, Gong Y, Zhang Y, et al. Facile synthesis of carbon nanosphere/NiCo2O4 core-shell sub-microspheres for high performance supercapacitor. *Sci Rep* 2015;5:12903. DOI PubMed PMC
45. Zhang Q, Chen H, Han X, et al. Graphene-Encapsulated nanosheet-assembled zinc-nickel-cobalt oxide microspheres for enhanced lithium storage. *ChemSusChem* 2016;9:186-96. DOI
46. Zhang Q, Wang J, Dong J, et al. Facile general strategy toward hierarchical mesoporous transition metal oxides arrays on three-dimensional macroporous foam with superior lithium storage properties. *Nano Energy* 2015;13:77-91. DOI
47. Li S, Wang K, Zhang G, et al. Fast charging anode materials for lithium-ion batteries: current status and perspectives. *Adv Funct Materials* 2022;32:2200796. DOI
48. Joy R, Balakrishnan NTM, Das A, et al. Graphene: chemistry and applications for lithium-ion batteries. *Electrochem* 2022;3:143-83. DOI